REPORT DOCUMENTATION PAGE

Dist: A

Public reporting burden for this collection of information is estimated to average 1 hour per response, including the time for reviewing instructions, searching existing data sources, gathering and maintaining the data needed, and completing and reviewing the collection of information. Send comments regarding this burden estimate or any other aspect of this collection of information, including suggestions for reducing this burden, to Washington Headquarters Services, Directorate for Information Operations and Reports, 1215 Jefferson Davis Highway, Suite 1204, Arlington, VA 22202-4302, and to the Office of Management and Budget, Paperwork Reduction Project (0704-0188), Washington, DC 20503.

1. AGENCY USE ONLY (Leave blank)	2. REPORT DATE	3. REPORT TYPE AND DATES COVERED
	2 December 1994	Final Report: 01 Dec 91 to 30 Nov 93

4. TITLE AND SUBTITLE
Numerical Investigation of Surface Curvature Effects
in Compressible Turbulent Flows

5. FUNDING NUMBERS
C- F49620-92-C-0012
2307/AS

6. AUTHOR(S)
Linda D. Kral
John F. Donovan

DTIC
ELECTE
JAN 31 1995
S G D

7. PERFORMING ORGANIZATION NAME(S) AND ADDRESS(ES)
McDonnell Douglas Aerospace
MC 1067126
P.O. Box 516
St. Louis, MO 63166-0516

8. PERFORMING ORGANIZATION REPORT NUMBER
MDC 94X0041
AFOSR- 95 0052

9. SPONSORING/MONITORING AGENCY NAME(S) AND ADDRESS(ES)
AFOSR/NA
Building 410
Bolling AFB DC 20332-6448

NA

10. SPONSORING/MONITORING AGENCY REPORT NUMBER
F49620-92-
C-0012
2307/AS

11. SUPPLEMENTARY NOTES

12a. DISTRIBUTION/AVAILABILITY STATEMENT

Approved for public release; distribution is
unlimited

12b. DISTRIBUTION CODE
A

13. ABSTRACT (Maximum 200 words)

The objective of this work has been to develop a direct numerical simulation capability for compressible, non-canonical wall-bounded flows which is directly applicable to actual flight vehicles. Data from the simulations is used to educe information about the organised motions in the flow and how they are affected by the extra strain rates due to concave wall curvature. A second-order finite volume approach and both fourth-order and sixth-order compact differences are available for the spatial derivatives. The algorithm allows for generalised coordinates so that simulations about complex geometries can be performed. Extensive testing was done for two subgrid-scale models, the compressible Smagorinsky and structure function models, for a supersonic boundary layer. As the subgrid-scale viscosity also behaves as an artificial viscosity for central differencing codes, the study reinforced the need for high-order dissipation models in the simulation code. Validation of the numerical method was performed for flow over a concave surface for subsonic flow in which streamwise vortices develop in the boundary-layer due to the Görtler instability. The geometry and flow conditions closely approximated the incompressible experiments of Swearingen and Blackwelder. The simulations captured the essential features of the experiments in which counter-rotating vortices developed near the wall. As these streamwise vortices develop, the laminar boundary layer on the concave wall rapidly becomes three-dimensional. Higher-momentum fluid is pulled towards the wall from the outer flow as vortices grow downstream. The low-speed fluid lying between the vortices induces low-momentum fluid away from the wall, leading to inflectional streamwise velocity profiles, in good agreement with the experiments.

DTIC QUALITY INSPECTED 3

14. SUBJECT TERMS
Compressible Turbulence; Compressible Transition; Large-Eddy
Simulation; Direct Numerical Simulation; Gortler Instability

15. NUMBER OF PAGES
32

16. PRICE CODE

17. SECURITY CLASSIFICATION OF REPORT	18. SECURITY CLASSIFICATION OF THIS PAGE	19. SECURITY CLASSIFICATION OF ABSTRACT	20. LIMITATION OF ABSTRACT
Unclassified	Unclassified	Unclassified	UL

NSN 7540-01-280-5500

19950127 079

PREFACE

The work reported here was performed by McDonnell Douglas Corporation in St. Louis, Missouri, for the United States Air Force Office of Scientific Research, Bolling Air Force Base, Washington, DC, under Contract F49620-92-C-0012. The work reported was conducted from 1 December 1991 to 30 November 1993. The principal investigators are Dr. L. D. Kral and Dr. J. F. Donovan.

The technical report has been reviewed and approved.

R. R. Cosner
Group Manager Engineering, MDC Fellow – Computational Fluid Dynamics
McDonnell Douglas Aerospace

F. W. Spaid
Group Manager Engineering – Experimental Fluid Dynamics
McDonnell Douglas Aerospace

R. N. Yurkovich
Manager Engineering, MDC Fellow – Advanced Flight Technologies
McDonnell Douglas Aerospace

Accesion For		
NTIS CRA&I		☒
DTIC TAB		☐
Unannounced		☐
Justification		
By		
Distribution /		
Availability Codes		
Dist	Avail and / or Special	
A-1		

Contents

List of Pages

TITLE PAGE

REPORT DOCUMENTATION PAGE

i – iv

1 – 32

List of Figures

1 OBJECTIVES

The objective of this research effort was to develop direct numerical simulation (DNS) and large-eddy simulation (LES) techniques to simulate compressible, non-canonical wall-bounded flows which are more directly applicable to actual flight vehicles. The data from the simulations is used to educe information about the organized motions in the flow and how they are affected by the extra strain rates due to the wall curvature. Also, the data from the simulations can be used for improvements to the Reynolds stress transport equations and the two-equation $k - \epsilon$ turbulence models for compressibility and curvature effects. Specifically, the research objectives are the following:

- Develop a high-order compact difference algorithm for solution of the compressible, Navier-Stokes and energy equations for simulation of spatially evolving three-dimensional turbulent flow.

- Investigate boundary condition compatibility issues and dissipation models for the higher-order differencing.

- Validate the code for small amplitude disturbances.

- Evaluate subgrid-scale models for wall-bounded compressible flows.

- Compute the turbulent flow over a flat plate at a supersonic Mach number and compare with incompressible simulations.

- Compute the transitional flow over a concave surface.

- Characterize the nonlinear stages of transition to determine the effects of the extra strain rates applied by the curved surface.

2   GOVERNING EQUATIONS

2.1   Governing Equations

The compressible transitional and turbulent flow of an ideal gas is governed by the continuity, momentum and energy equations. The strongly conservative form of these governing equations will be solved. The equations can be written as follows, where $u_k = [u, v, w]^T$ is the velocity and ρ, p, T, μ, κ, and C_v are the density, pressure, temperature, viscosity, thermal conductivity, and specific heat at constant volume respectively:

$$\frac{\partial \rho}{\partial t} + \frac{(\partial \rho u_k)}{\partial x_k} = 0 \tag{1}$$

$$\frac{\partial (\rho u_k)}{\partial t} + \frac{\partial (\rho u_k u_l)}{\partial x_l} = -\frac{\partial p}{\partial x_k} + \frac{\partial \sigma_{kl}}{\partial x_l} \tag{2}$$

$$C_v \frac{\partial(\rho T)}{\partial t} + C_v \frac{\partial(\rho u_k T)}{\partial x_k} = -p\frac{\partial u_k}{\partial x_k} + \frac{\partial}{\partial x_k}\left(\kappa \frac{\partial T}{\partial x_k}\right) + \Phi \tag{3}$$

The viscous stress σ_{kl} and the viscous dissipation Φ are defined by

$$\sigma_{kl} = -\frac{2}{3}\mu \frac{\partial u_j}{\partial x_j}\delta_{jl} + \mu\left(\frac{\partial u_k}{\partial x_l} + \frac{\partial u_l}{\partial x_k}\right) \tag{4}$$

$$\Phi = -\frac{2}{3}\mu\left(\frac{\partial u_j}{\partial x_j}\right)^2 + \mu\left(\frac{\partial u_k}{\partial x_l} + \frac{\partial u_l}{\partial x_k}\right)\frac{\partial u_k}{\partial x_l}. \tag{5}$$

The equation of state is

$$p = \rho RT. \tag{6}$$

The viscosity and thermal conductivity are varied with temperature using Sutherland's law for the viscosity and a fourth–order polynomial curve fit to experimental data for the thermal conductivity. The specific heat at constant volume is assumed constant. The physical domain (x, y, z) is mapped to the computational domain (ξ, η, ζ) to allow for arbitrarily shaped bodies.

2.2   Favre Filtered Equations

In LES the flow variables are decomposed into a large–scale component and a subgrid–scale component. The large–scale component is defined by a filtering operation:

$$\overline{\mathcal{F}}(x_1, x_2, x_3) = \int_D \prod_{i=1}^{3} G_i(x_i, x_i') f(x_1', x_2', x_3')\, dx_1' dx_2' dx_3' \tag{7}$$

where G_i is a filter function in the ith direction and D is the domain of the fluid. Two commonly used filters are the sharp Fourier cutoff filter, defined in physical space as

$$G_i(x_i, x_i') = 2 \sin\left[\pi\left(x_i - x_i'\right)/\Delta_i\right]/\pi\left(x_i - x_i'\right) \qquad (i = 1, 3) \tag{8}$$

and the Gaussian filter defined as

$$G_i(x_i, x_i') = (6/\pi\Delta_i)^{1/2} \exp\left[-6\left(x_i - x_i'\right)^2/\Delta_i^2\right] \qquad (i = 1, 3) , \tag{9}$$

where Δ_i is proportional to the grid size in the ith direction. For the Fourier cutoff filter the subgrid scale field contains the velocity due to all the structures with wavenumber $|k_i| > \pi/\Delta_i$. The Gaussian filter is a more global filter since a wider range of scales contribute to the subgrid–scale velocity.

Favre filtering is used to decompose the turbulent field: $\mathcal{F} = \tilde{\mathcal{F}} + \mathcal{F}'$, where $\mathcal{F}'$ is the SGS part of $\mathcal{F}$ and the Favre filter is defined by $\tilde{\mathcal{F}} = \overline{\rho\mathcal{F}}/\overline{\rho}$. The filtering operation is applied to the governing equations which yields filtered equations for the large eddies:

$$\frac{\partial\overline{\rho}}{\partial t} + \frac{\partial(\overline{\rho}\tilde{u}_k)}{\partial x_k} = 0 \tag{10}$$

$$\frac{\partial(\overline{\rho}\tilde{u}_k)}{\partial t} + \frac{\partial(\overline{\rho}\tilde{u}_k\tilde{u}_l)}{\partial x_l} = -\frac{\partial\overline{p}}{\partial x_k} + \frac{\partial\tilde{\sigma}_{kl}}{\partial x_l} + \frac{\partial\tau_{kl}}{\partial x_l} \tag{11}$$

$$C_v\frac{\partial(\overline{\rho}\tilde{T})}{\partial t} + C_v\frac{\partial(\overline{\rho}\tilde{u}_k\tilde{T})}{\partial x_k} = -\overline{p}\frac{\partial\tilde{u}_k}{\partial x_k} + \tilde{\Phi} + \frac{\partial}{\partial x_k}\left(\tilde{\kappa}\frac{\partial\tilde{T}}{\partial x_k}\right) - C_v\frac{\partial Q_k}{\partial x_k} \tag{12}$$

$$\overline{p} = \overline{\rho}R\tilde{T} . \tag{13}$$

The SGS stress tensor τ_{kl} and the SGS heat flux Q_k are defined by

$$\tau_{kl} = -\overline{\rho}(\widetilde{\tilde{u}_k\tilde{u}_l} - \tilde{u}_k\tilde{u}_l + \widetilde{u_k'\tilde{u}_l} + \widetilde{u_l'\tilde{u}_k} + \widetilde{u_k'u_l'}) \tag{14}$$

$$Q_k = \overline{\rho}(\widetilde{\tilde{u}_k\tilde{T}} - \tilde{u}_k\tilde{T} + \widetilde{u_k'\tilde{T}} + \widetilde{\tilde{u}_kT'} + \widetilde{u_k'T'}). \tag{15}$$

2.3 Subgrid–Scale Modeling

The capabilities of two SGS stress models to accurately model wall–bounded, compressible, turbulent flows are investigated. The SEZHu model and the structure function model are chosen due to their success in modeling the SGS physics of compressible isotropic turbulence. A brief description of these models follows.

The SEZHu SGS model was derived by Speziale *et al.* (1988) for compressible isotropic turbulence. This model is based on the Favre-filtered equations of motion of an ideal gas.

Piomelli *et al.* (1988) has shown that the structure of the subgrid scales depends strongly on the type of filter used and consistency between the model and filter is necessary for accurate results. Following the work of Piomelli *et al.* (1988), only the Smagorinsky portion of the SEZHu model is used with the Fourier cutoff filter. Hence, the SGS stress model is of the form

$$\tau_{kl} = \left(1 - e^{-y^+/25}\right)^2 2\, C_R\, \overline{\rho}\, \Delta^2\, II_{\tilde{S}}^{1/2} \left(\tilde{S}_{kl} - \frac{1}{3}\tilde{S}_{mm}\delta_{kl}\right) \tag{16}$$

and the SGS heat flux is given by

$$Q_k = \left(1 - e^{-y^+/25}\right)^2 \overline{\rho} \left(-\frac{C_R}{Pr_T}\Delta^2 II_{\tilde{S}}^{1/2}\frac{\partial \tilde{T}}{\partial x_k}\right) \tag{17}$$

where $\tilde{S}_{kl} = \left(\partial \tilde{u}_k/\partial x_l + \partial \tilde{u}_l/\partial x_k\right)/2$ is the Favre filtered rate of strain tensor and $II_{\tilde{S}} = \tilde{S}_{mn}\tilde{S}_{mn}$ is its second invariant. C_R is the compressible Smagorinsky constant, Pr_T is the turbulent Prandtl number, and $\Delta = (\Delta x \Delta y \Delta z)^{1/3}$. The first term in these equations represents a Van Driest wall damping and y^+ is the distance from the wall nondimensionalized by wall shear velocity and kinematic viscosity.

The second SGS model is the structure function model (Comte *et al.* 1990) which is based on the concept of spectral eddy viscosity and spectral eddy diffusivity. A local kinetic energy spectrum is calculated in terms of the local second–order velocity structure function. The structure function model is of the following form for the SGS shear stress and heat flux:

$$\tau_{kl} = \left(1 - e^{-y^+/25}\right)^2 C_R\, \overline{\rho}\, \Delta \sqrt{\overline{F}_2\left(\vec{x}, \Delta x, t\right)} \times \left(\tilde{S}_{kl} - \frac{1}{3}\tilde{S}_{mm}\delta_{kl}\right) \tag{18}$$

$$Q_k = \left(1 - e^{-y^+/25}\right)^2 \left(-\frac{C_R\overline{\rho}\Delta}{Pr_T}\sqrt{\overline{F}_2\left(\vec{x}, \Delta x, t\right)}\frac{\partial \tilde{T}}{\partial x_k}\right) \tag{19}$$

where

$$\overline{F}_2 = \left\langle \|\vec{u}(\vec{x},t) - \vec{u}(\vec{x} + \vec{r}, t)\|^2 \right\rangle_{\|\vec{r}\|=\Delta x}. \tag{20}$$

Again, Van Driest wall damping is applied.

3 NUMERICAL APPROACH

A large extent of this research effort has been directed towards development of the development of the high-order compact difference simulation code for generalized curvilinear coordinates, as outlined in the objectives. Towards this end, several studies were performed to determine the most appropriate numerical techniques. The numerical algorithm and several key numerical issues are highlighted below, including application to specific test cases.

For the time integration scheme, the second-order Runge-Kutta methods by Jameson (1980), the low storage third-order Runge-Kutta methods by Wray (1991) and Williamson (1980), and the classical fourth-order Runge-Kutta method have been evaluated. The third- and fourth-order schemes were tested for a simple ordinary differential equation and the predicted third- or fourth-order accuracy was achieved. The third-order Runge-Kutta method requires fewer computations and less storage than the fourth-order Runge-Kutta method and is being used in the full simulations.

For the spatial differencing procedure, a second-order finite volume approach and fourth-order or sixth-order compact differences are available. A generalized coordinate system is being used to allow for arbitrarily shaped bodies. A cell-centered scheme is employed for the second-order finite volume method. The compact difference scheme is applied at the nodes, not the cell centers, since higher order interpolation schemes would be required for a cell-centered scheme, resulting in many additional calculations.

Both the fourth-order and sixth-order compact differences form a tridiagonal system of equations. The difference approximations for the near boundary nodes are necessarily one-sided and consistent with the overall compact difference scheme. Following the work of Lele (1990), Carpenter (1991) and Pruett(1993), the following schemes are employed at the boundaries. For the fourth-order compact differences, a 3–4–3 stencil is used, which represents fourth-order differencing in the interior of the mesh and third-order at the boundaries. For the sixth-order compact differences, either a 3,4–6–4,3 stencil or a 5,5–6–5,5 stencil is used in which sixth order compact differences are used in the interior. For the first method, third-order compact differences are used at the boundaries and fourth-order differences are used at the first interior points. Similarly, the second sixth-order method employs fifth-order differences at the boundaries and the first interior points. The code is programmed so that either set of boundary conditions can be used for the sixth-order compact differences. However, Pruett has shown that stability is maintained when the 5,5–6–5,5 scheme is used in the streamwise direction and the 3,4–6–4,3 scheme is used in the wall-normal direction. Therefore, the boundary values are formally fifth-order accurate in the streamwise direction since the points are equally spaced. However, only third-order accuracy is maintained in the wall-normal direction where the grid points are tightly clustered or highly stretched.

The spatial evolution of the transitional and turbulent flowfield is simulated since this is the only physically representative condition for complex geometries. Inflow-outflow boundary conditions are employed. At the inflow boundary, the flow is assumed to be a uniform freestream flow is the leading edge of the body is simulated; otherwise a boundary layer profile is used at the inflow boundary. At the outflow and outer boundaries, characteristic boundary conditions are employed.

In the spanwise direction, periodic boundary conditions are employed in the finite difference or compact difference framework. At the wall, no-slip conditions are imposed, the temperature is calculated from an adiabatic wall condition, and either a zero-normal gradient in the pressure is assumed or continuity is imposed at the wall. The equation of state is also employed to calculate either the density or pressure.

A fourth-order artificial dissipation operator has been added to the second-order finite-volume formulation to damp spurious oscillations. A spatial filter was developed for near-boundary damping. No dissipation operator has yet been added to the higher-order compact differencing scheme, but a sixth-order filtering is planned so that reasonable grids can be used.

Disturbances can be introduced into the computational domain either through a suction/blowing strip on the wall or as a distributed function at the inflow boundary.

4   NUMERICAL VALIDATIONS

4.1   Burger's Equation

Both the fourth-order compact differences and second-order finite differences for the spatial derivatives have been tested for a model problem. A comparison of fourth-order compact differencing techniques with second-order finite difference techniques was performed for Burger's equation. It was found that the boundary condition treatment has a significant impact on the order of accuracy of the numerical solution. The behavior of compact difference techniques is similar to that of spectral methods in that a larger region of the flowfield is affected by the boundary condition treatment and the error distribution is more global. The errors are more local to regions of high gradients in the finite-difference solution. In addition, round-off errors can become larger than the truncation error for small grids and thus reduce the effectiveness of the higher-order differencing. As compact differencing techniques have additional CPU requirements, there may not be a payoff for a very fine grid. The results from the analysis of Burger's equation have provided useful information for the complete Navier-Stokes equations and highlights of some of the test cases are given below.

The first analysis is for the linear, steady, viscous solution of Burger's equation with Dirichlet boundary conditions imposed:

$$c\frac{\partial u}{\partial x} = \frac{1}{Re}\frac{\partial^2 u}{\partial x^2} \tag{21}$$

$$u(0) = 1, \qquad u(1) = 0, \qquad c = 1, \qquad Re = 10.$$

Figure 1 shows the rms error in the calculated solution when compared with the exact solution of Burger's equation using standard second-order central differences and fourth-

order compact differences. The slope of the curves verify the solution accuracy, except at the smaller step sizes when the round-off error overtakes the truncation error. Figure 2 shows the spatial distribution of the error for four different size uniform grids. The error in the second-order finite difference solution is very large at the boundary, but decreases for the smaller step sizes as expected (imax indicates the number of grid points used in the computation). The error in the fourth-order compact difference solution (with a fourth-order one-sided difference for the first derivative and a third-order one-sided difference for the second derivative at the boundary) does not change as the grid size is reduced since the round-off error is higher than the truncation error for these smaller grids.

A second analysis was performed to determine the effects of periodic boundary conditions for the unsteady, viscous Burger's equation ($c = 1$ and $Re = 6283$). The error analysis is shown in Figure 3 for both the finite difference and compact difference solutions. The results display that second- and fourth-order accuracy is achieved. Unlike the previous case, no error is introduced at the boundaries. As periodic boundary conditions are being employed in the spanwise direction in the full simulation code, this study lends confidence to the capabilities of the differencing techniques employed.

Another analysis of the steady, nonlinear, viscous Burger's equation, which more closely models the characteristics of the Navier-Stokes equations, was performed. The same conditions were used as presented in the first example, but with $c = u$. The error is shown in Figure 4. The finite difference solution shows second-order accuracy, while the compact difference solution only maintains a 3.5 order accurate solution as the step size is reduced. The accuracy of the compact difference solution was degraded from fourth-order because the the third-order boundary condition for the second derivative influenced the flow more for the nonlinear Burger's equation. For very coarse grids, the accuracy of the compact difference solution is no better than the second-order finite difference solution.

The final example of the analysis of Burger's equation is for the unsteady, combined nonlinear, viscous case:

$$\frac{\partial u}{\partial t} + (c + b\, u)\frac{\partial u}{\partial x} = \frac{1}{Re}\frac{\partial^2 u}{\partial x^2} \tag{22}$$

$$u(0,t) = 1, \qquad u(1,t) = 0, \qquad c = 0.5, \qquad b = -1, \qquad Re = 10\,.$$

The solution of this equation is shown in Figure 5 and the error distribution is shown in Figure 6. Of particular interest is the more localized concentration of error for the finite difference solution, whereas the errors in the compact difference solution are spread over a larger portion of the domain, similar to the error distributions seen in spectral methods. A grid density study showed that second-order accuracy was achieved for the finite difference solution and fourth-order accuracy for the compact difference solution. This test case lends

confidence to the higher-order differencing techniques used in the calculation of flows with large gradients, as will be present in the full simulations of supersonic turbulent flow over a curved surface.

The results presented for Burger's equation were obtained on a uniform grid. However, the grid can play a large role in the overall accuracy of the simulation. Special care is taken to preserve the higher-order accuracy of the numerical scheme. The grid generation for the generalized code is accomplished through the MACGS grid generation system developed by the Computational Fluid Dynamics Group at McDonnell Douglas Aerospace. The grid stretching is performed at a small, constant rate, as this yields smaller errors than if a *tanh* stretching were used. As Cain (1992) has pointed out, when using second- and higher-order schemes to calculate the metrics, the metrics will be exact on this type of grid. Also, Cain has determined maximum stretching rates based on the one-dimensional wave equation. If the stretching is too large, the waves can propagate in the wrong direction. The metric calculation is implemented to be consistent with the order of accuracy of the flow solver scheme.

4.2   Mean Flow

Direct or large-eddy simulation methods require very accurate resolution of the underlying mean flow to capture the physics of transitional or turbulent flows. Great care has been taken to insure that the laminar mean flow solutions are of high accuracy. Comparison has been made between the results of the code developed in this work and the compressible similarity solution. The computational domain did not contain the leading edge of the plate and the compressible similarity solution was used as an inflow condition and to initialize the flowfield. A comparison between the compressible similarity solution and the newly developed code for a $M_\infty = 3$ supersonic boundary layer is shown in Figure 7 for the streamwise u velocity, the normal v velocity, and the temperature T. Excellent agreement is obtained, particularly for the normal v velocity.

5   SIMULATION RESULTS

5.1   Large-Eddy Simulation of Supersonic Boundary Layers

An investigation of SGS models for use in compressible wall bounded flows was performed using a temporal LES code, CMPTBL (CoMPressible, Temporal, Boundary Layer), developed by Pruett and Zang (1992). This code was used to perform the first LES of supersonic, wall-bounded turbulent flow (Kral and Zang, 1992). However, there several outstanding issues concerning SGS models for supersonic boundary layers arose. This work was therefore

continued in a cooperative effort with Dr. Thomas A. Zang at NASA Langley Research Center. As the temporal code requires much less CPU time (due to the streamwise periodicity approximation) it provided a good framework to examine key numerical issues while the fully spatial code was under development. The subgrid-scale viscosity can behave similar to an artificial viscosity operator for central differencing codes. As there is no artificial viscosity or upwinding technique in CMPTBL, the values of the compressible constant in the SGS models were set high to provide damping of unphysical oscillations. Since the earlier work by Kral and Zang (1992), Zang (1992) has made several modifications that improved stability and provided for more physical damping. These modifications included treating the viscous terms directly as second derivatives instead of products of first derivatives. In the previous work, the differencing of the product of the first derivatives did not damp the high frequency waves. This modification provided for a much more stable algorithm for temporal simulations of transition with no affect on the solution. In addition, boundary condition upgrades for the sixth-order compact differences used in the wall normal direction were made.

Therefore, the earlier findings on the SGS models were re-examined, especially the influence of the compressible constant. Two SGS models with compressible formulations were evaluated. One model is a compressible formulation of the Smagorinsky model due to Speziale *et al.* (1988) and the second model is the structure function model of Comte *et al.* (1990). Significant differences were observed in the magnitude and shape of the fluctuating components using the two different SGS models. Figure 8 shows a comparison between results of a LES with the compressible Smagorinsky SGS model at $M_\infty = 4.5$ and $Re_\theta = 5400$ using the earlier version of the code (labeled 8/91 on the plot) and the current version (labeled 7/92 on the plot). Also shown is a comparison with the experimental data of Coles (1953) at this Mach number and Re_θ. All simulations presented here were run with 32 Fourier modes in the streamwise direction, 18 Fourier modes in the half-span (with spanwise symmetry assumed), and 72 points in the wall-normal direction using sixth-order compact differencing. The same Smagorinsky constant was used in both cases, $c_r = 0.15$. Differences in the two simulations are most evident in the near wall region for the first derivative of the mean streamwise velocity and for u'_{rms}. The differences between these two cases were not expected to be significant. The intention was to attempt to lower c_r with the more stable numerical scheme implemented for the second derivatives, as the constant was set high due to the need for artificial dissipation. With the modifications, c_r was lowered by 50% to 0.075. Thus the need for artificial dissipation is not as high in the current version of CMPTBL. Results with the lower values of c_r are shown in Figure 9. The slope of the mean velocity and temperature changes significantly at the wall. With the decrease in c_r, the SGS viscosity is reduced, which leads to higher values for u'_{rms}. Similar results were found for the structure

function SGS model and results are shown in Figure 10. The constant c_r was lowered by 30% from 0.30 to 0.21 before numerical stability became an issue.

As the *proper* value for this constant is not known for supersonic, wall-bounded turbulent flows, the results of these temporal simulations can be used as a guide in the spatial simulations.

Figure 11 shows results from the temporal LES of supersonic turbulent flow over a flat plate at $M_\infty = 4.5$. Shown is a constant density surface at one instant in the simulation using the compressible Smagorinsky SGS model. The simulation appears to be modeling the important physics of the boundary layer as evidenced by the similarity of certain flow features to those observed in experiments. Horseshoe-shaped structures, visible in the figure, are almost identical to structures found in incompressible boundary layers (see, e.g. Robinson, 1991) and are very similar to those observed in compressible flows where much less experimental information is available (Spina et al., 1991). Additional visualization of low momentum fluid near the wall, as shown in Figure 12 indicates low-speed streaks and shows regions of these streaks lifting away from the wall in the vicinity of the horseshoe-like structures, as observed experimentally. In Figure 13, contours of density at a spanwise plane in the boundary layer are shown, convecting with $0.85U_e$ which is the approximate convection speed of large-scale motions. Superimposed are velocity vectors. Low density fluid is lifted up from the wall and local shear layers are observed away from the wall that are associated with the low-density structures. The downstream "bulge" is in early stages of development as depicted by the strong shear layers seen on the upstream side. The results are in qualitative agreement with incompressible motions.

5.2   Direct Numerical Simulation of Görtler Flow

Counter-rotating streamwise vortices are observed in transitional and turbulent boundary layers and play an important role in the dynamics governing the dynamics governing the growth, breakdown, and transition to turbulence. The streamwise vortices develop in boundary-layer flow over a concave wall due to the imbalance of the centrifugal forces and the radial pressure gradient as first predicted by Görtler (1940). As this Görtler instability is a common phenomena in various flows involving curved boundaries, it was chosen to be our validation case for the numerical method developed to date.

The geometry and flow conditions closely approximate the incompressible experiments of Swearingen and Blackwelder (1987). A sketch of the streamwise vortices developing on a concave wall is shown in Figure 14. The spanwise wavelength of the vortices is denoted by

λ in the figure. The governing nondimensional parameter is Görtler number defined by

$$Go_\theta = \frac{U_\infty \theta}{\nu}\sqrt{\frac{\theta}{R}} = Re_\theta\sqrt{\frac{\theta}{R}}$$

where θ is the momentum thickness, U_∞ is the freestream velocity, R is the radius of curvature, and ν is the kinematic viscosity. In contrast to the experiments, the simulations were performed at $M_\infty = 0.5$ in order to validate the code at subsonic Mach numbers. The radius of curvature is $R = 3.2\ m$, the freestream velocity is $U_\infty = 174\ m/s$, the freestream temperature is $T = 300\ K$, the unit Reynolds number per meter is $Re = 3.2 \times 10^5\ m^{-1}$, and the streamwise length of the computational domain is $L = 251\ cm$. The spanwise wavelength is chosen to match the experimentally observed wavelength, $\lambda = 2.3\ cm$. The flow is unstable for $Go_\theta > 0.3$ and the critical value for transition to turbulence occurs between $6 < Go_\theta < 10$ or $78\ cm < x < 152\ cm$. The disturbance is introduced into the computational domain at the inflow boundary through the introduction of perturbations in the spanwise and wall-normal velocities.

The grid for this direct simulation was generated using MACGS, with constant stretching in the streamwise direction and constant spacing in the spanwise direction. A small, constant rate stretching is used in the wall normal direction. The computational grid is shown in Figure 15. The grid is $104 \times 61 \times 31$. Curvature starts at the leading edge and the computational domain extends from $5\ cm$ upstream of the leading edge to $251\ cm$ downstream of the leading edge along the surface. The spanwise extent of the domain is $2.3\ cm$ corresponding to one wavelength.

The initial stages of this instability exhibit the expected exponential growth in the streamwise direction. Figure 16 shows the downstream growth of the amplitude of the spanwise velocity near the wall at a value of $y^+ \approx 10$. The disturbance has propagated to $110\ cm$ and the flowfield downstream of this location is not yet developed.

Normal profiles of the mean streamwise velocity at five downstream locations are shown in Figure 17 for spanwise locations corresponding to a peak and a valley region. A 'peak' is the region where $u'(z)$ is a maximum and $U(z)$ is a minimum. A noticeable distortion of the mean laminar flow is observed in the figure. The peak region shows a velocity defect and the valley region shows an increase in the mean velocity. Concentrated regions of low- and high-speed fluid are produced and the boundary layer has a wavy appearance in the spanwise direction. In the low-speed region at $x = 80\ cm$, the mean velocity profile is inflectional in the normal y direction. The inflectional profiles indicate the imminent onset of a tertiary instability and the breakdown to turbulence. The mean streamwise profiles are in agreement with the experiments of Swearingen and Blackwelder (1987), in which the inflectional profile was observed also at $x = 80\ cm$.

The low- and high-speed regions in the spanwise direction results in an alternating increase and decrease in the thickness of the boundary layer. The calculated development of the displacement thickness δ^* in the downstream direction for the low- and high-speed regions is compared with the laminar growth in Figure 18. Also shown are the measurements of Swearingen and Blackwelder. In the low-speed region, δ^* increases dramatically near $x = 40\ cm$. A corresponding decrease in δ^* is observed in the high-speed region. Again, the Görtler instability has reached about $x = 110\ cm$ in the simulations. Overall, the agreement between the calculations and the experiments is quite good.

The growth of the vortex system is illustrated in Figure 19. Iso-contours of the streamwise velocity are shown at several downstream locations. Also shown is a comparison with the experiments of Swearingen and Blackwelder at the same locations. Initially the disturbances are linear and the boundary layer appears unperturbed, but is quickly modified downstream, as the disturbance becomes non-linear and the influence of the counter-rotating vortices is evident. As low-momentum fluid is pumped away from the wall between vortices, the boundary layer and on either side of the domain the boundary layer is thinned due to the induction of fluid towards the wall. The comparison between the direct numerical simulations and the experiments is qualitatively similar. However, it appears that the development of the Görtler vortices in the simulations is delayed $10 - 20\ cm$ relative to the experiments. This result is not unexpected because factors present in the experiment, such as surface roughness and possibly larger amplitude disturbances, will cause the boundary layer to be less stable.

Streamwise vortices initiated by the Görtler instability exist in the presence of a strong mean gradient of the streamwise velocity $U(y)$. Between the two vortices, the induced motion removes low-momentum fluid away from the wall. At one-half wavelength away in the spanwise direction, the vortices pump high-speed fluid towards the wall. The counter-rotating vortices are illustrated in Figure 20, which shows contours of spanwise velocity. The low-speed regions that result from this lift-up of low-momentum fluid develop inflectional velocity profiles as shown in Figure 17.

Although these simulations have not yet reached a fully turbulent state, at the time of this report the Görtler instability is still proceeding downstream. It is anticipated that the final breakdown to turbulence will occur.

6   SUMMARY

The objective of this work has been to develop a DNS capability for compressible, non-canonical wall-bounded flows which is directly applicable to actual flight vehicles. A significant part of this effort was placed on the development of the numerical algorithm that is used to perform DNS of compressible, turbulent flows over bodies with surface curvature.

Much of the work has therefore focused on resolving issues necessary in formulating the numerical method. A second-order finite volume approach and both fourth-order and sixth-order compact differences are available for the spatial derivatives. A third-order low-storage Runge-Kutta scheme is used for the time integration. The algorithm allows for generalized coordinates so that simulations about complex geometries can be performed. Extensive testing was performed for two SGS models, the compressible Smagorinsky and structure function models, to determine the effects of the SGS constant. The study reinforced the need for high-order dissipation models in the simulation code, as the SGS viscosity also behaves as an artificial viscosity for central differencing codes. The numerical method was validated for flow over a concave surface at $M_\infty = 0.5$ in which streamwise vortices develop in the boundary-layer due to the Görtler instability. The geometry and flow conditions closely approximated the experiments of Swearingen and Blackwelder (1987). The simulations captured the essential features of the experiments in which counter-rotating vortices developed near the wall. The laminar boundary layer on the concave wall rapidly becomes three-dimensional as these streamwise vortices develop. The vortices grow downstream and higher-momentum fluid is pulled towards the wall from the outer flow. The low-speed fluid lying between the vortices induces low-momentum fluid away from the wall, leading to inflectional streamwise velocity profiles, in good agreement with the incompressible studies of Swearingen and Blackwelder.

7 REFERENCES

Cain, A. B., 1992, *Private Communication.*

Carpenter, M. H., Gottlieb, D., & Abarbanel, S. 1991 "The Stability of Numerical Boundary Treatments for Compact High-Order Finite-Difference Schemes," ICASE Report No. 91-71.

Coles, D., 1953, "Measurements in the Boundary Layer on a Smooth Flat Plate in Supersonic Flow: I. The Problem of the Turbulent Boundary Layer, II. Instrumentation and Experimental Techniques at the Jet-Propulsion Laboratory, and III. Measurements in a Flat-Plate Boundary Layer at the Jet-Propulsion Laboratory," J. P. L. Cal. Inst. Tech. Rep. Nos. 20-69, 20-70, 20-71.

Comte, P, Lee, S., Cabot, W. H., 1990, "A Subgrid-Scale Model Based on the Second-Order Velocity Structure Function," Center for Turbulence Research, *Proc. of the Summer Program 1990*, pp. 31-45.

Görtler, H., 1940, "Über eine Dreidimensionale Instabilität Laminarer Grenzshichten an Konkaven Wänden," *Nachr. Wiss. Ges. Göttingen Math. Phys. Kl.*, **2**, pp. 1-26.

Jameson, A., Schmidt, W., and Turkel, E., 1981, " Numerical Solutions of the Euler Equations by Finite Volume Methods Using Runge-Kutta Time-Stepping Schemes," AIAA-81-1259.

Kral, L. D. and Zang, T. A., 1992, "Large-Eddy Simulation of Supersonic, Wall-Bounded, Turbulent Flows," *Proc. of the ICASE/LaRC Workshop on Transition and Turbulence*, Springer-Verlag, New York, 1992.

Lele, S. K. 1990 "Compact Finite Difference Schemes with Spectral-like Resolution," *J. Comp. Physics.*

Piomelli, U., Moin, P., and Ferziger, J. H. 1988 "Model Consistency in Large Eddy Simulations of Turbulent Channel Flows," *Phys. Fluids*, **31**, No. 7, pp. 1884-1891.

Pruett, C. D. and Chang, C.-L., 1993, "A Comparison of PSE and DNS for High-Speed Boundary-Layer Flows," *Proc. of the Symposium on Transitional and Turbulent Compressible Flows, ASME Fluids Engineering Conference*, Washington, D. C., June.

Pruett, C. D. and Zang, T. A., 1992, "Direct Numerical Simulation of Laminar Breakdown in High-Speed Axisymmetric Boundary Layers," AIAA-92-0742.

Robinson, S. K., 1991, "Coherent Motions in the Turbulent Boundary Layer," *Ann. Rev. Fluid Mech.*, **23**, pp. 601-639.

Speziale, C. G., Erlebacher, G., Zang, T. A., and Hussaini, M. Y., 1988, "The Subgrid-Scale Modeling of Compressible Turbulence," *Phys. Fluids*, **31**, No. 4, pp. 940-942, April.

Spina, E. F., Donovan, J. F., and Smits, A. J., 1991, "On the Structure of High-Reynolds Number Supersonic Turbulent Boundary Layers," *J. Fluid Mechanics*, **222**, pp. 293-327.

Swearingen, J. D. and Blackwelder, R. F., 1987, "The Growth and Breakdown of Streamwise Vortices in the Presence of a Wall," *J. Fluid Mechanics*, **182**, pp. 255-290.

Williamson, J. H., 1980, "Low-Storage Runge-Kutta Schemes," *J. Comp. Physics*, **35**, pp. 48-56.

Wray, A. A., 1991, "Minimal Storage Time-Advancement Schemes for Spectral Methods," *Private Communication per A. B. Cain.*

Zang, T. A., 1992, *Private Communication.*

8   PUBLICATIONS

Manuscripts planned for submission or submitted include:

(1) "Numerical Investigation of the Görtler Instability in a Compressible Flow," J. F. Donovan and L. D. Kral, submitted to the *Second Symposium on Transitional and Turbulent Compressible Flows*, ASME Fluids Engineering Conference, August 1995.

(2) "Higher-Order Numerical Techniques for Direct Numerical Simulation of Compressible Turbulent Flow over a Curved Surface," L. D. Kral and J. F. Donovan, most likely to be submitted to *Journal of Computational Physics*.

(3) "The Influence of Compressiblity on the Development of Streamwise Vortices," L. D. Kral and J. F. Donovan, most likely to be submitted to *Journal of Fluid Mechanics*.

(4) "Characterization of Turbulent Structure in a Supersonic Boundary Layer on a Curved Surface," J. F. Donovan and L. D. Kral, most likely to be submitted to *Journal of Fluid Mechanics*.

9   PROFESSIONAL PERSONNEL

This research has been conducted by:

Linda D. Kral, Ph.D., McDonnell Douglas Aerospace.

John F. Donovan, Ph.D., McDonnell Douglas Aerospace.

10   INTERACTIONS

(a) Conferences

"Direct Numerical Simulation of the Compressible Laminar-Turbulent Transition Process in Görtler Flow," L. D. Kral and J. F. Donovan, *47th Annual Meeting of the Division of Fluid Dynamics, American Physical Society*, Atlanta, Georgia, November 1994.

(b) Proceedings

"Large-Eddy Simulation of Supersonic, Wall-Bounded, Turbulent Flows," L. D. Kral and T. A. Zang, *Laminar-Turbulent Transition: ICASE/LaRC Workshop, Hampton, Virginia, 1991*, eds. M. Y. Hussaini, A. Kumar, and C. L. Streett, Springer-Verlag, New York, 1992, pp. 589-599.

(c) Seminars

"Numerical Simulation of Compressible Turbulent Flow," L. D. Kral, *Invited Seminar*, University of Illinois at Urbana-Champaign, Urbana, Illinois, April 1994.

"Numerical Simulation of Compressible Turbulent Flow," L. D. Kral, *Invited Seminar*, University of Missouri-Columbia, Columbia, Missouri, November 1993.

"Numerical Simulation of Compressible Turbulent Flow," L. D. Kral, *Invited Seminar*, Washington University, St. Louis, Missouri, November 1992.

(d) Government Interactions

Interacted informally with Dr. Thomas A. Zang at NASA Langley Research Center concerning numerical issues and subgrid-scale models.

Interacted informally with Dr. Charles D. Pruett of AS&M at NASA Langley Research Center concerning compact-differencing numerical issues.

11 DISCOVERIES, INVENTIONS, PATENT DISCLOSURES

None.

12   FIGURES
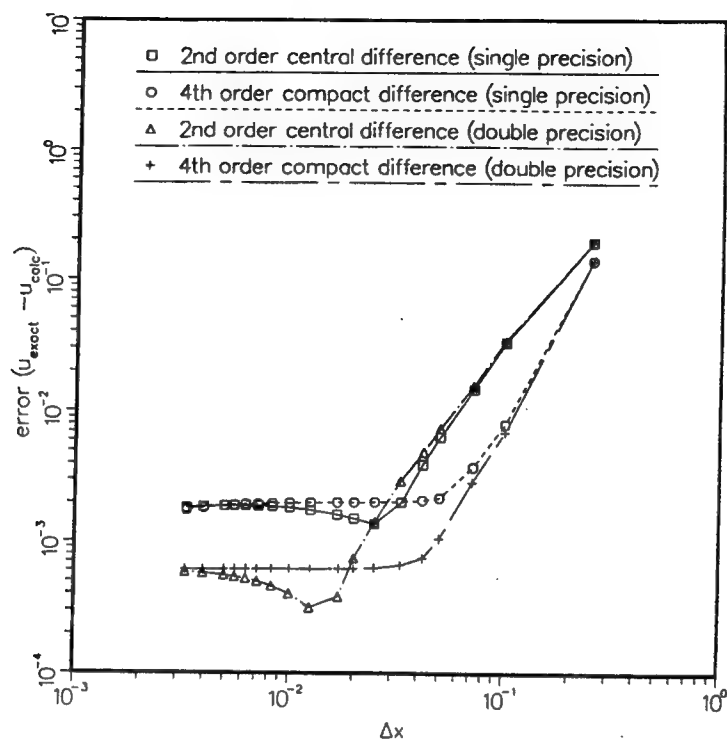
Figure 1: Rms error in computing the steady, linear, viscous Burger's equation at $Re = 10$ and $c = 1$ using second-order finite differences and fourth-order compact differences.
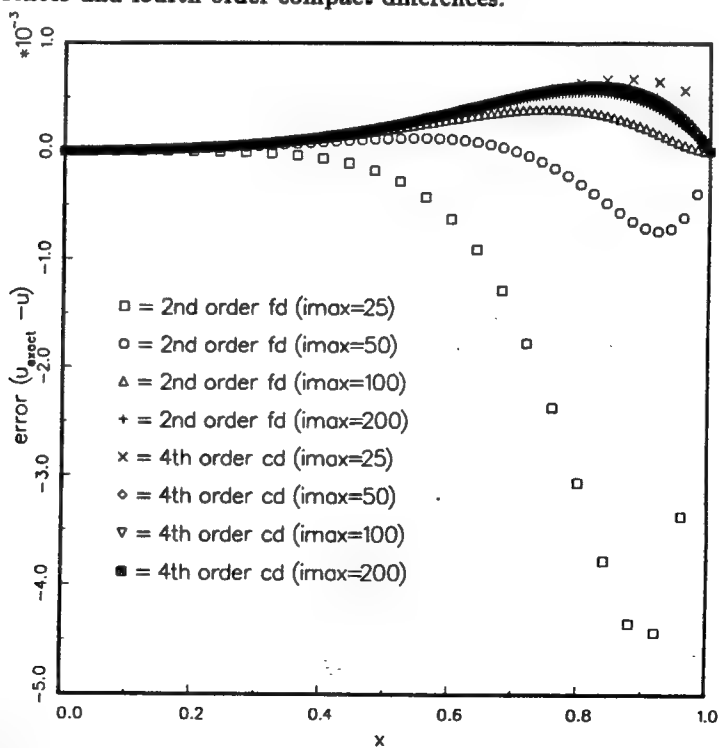
Figure 2: Spatial distribution of error for the steady, linear, viscous Burger's equation at $Re = 10$ and $c = 1$ using second-order finite differences and fourth-order compact differences for four different size uniform grids.
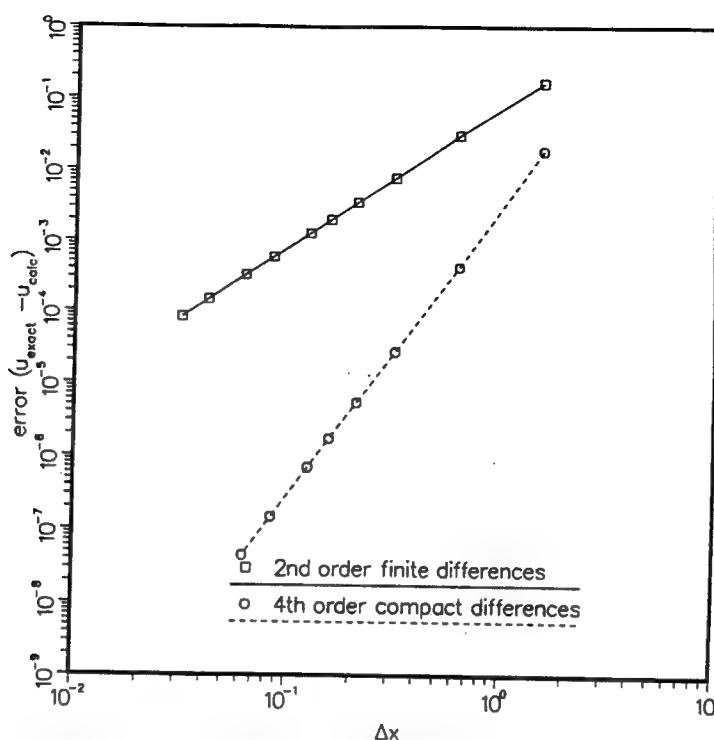
Figure 3: Rms error in computing the unsteady, linear, viscous Burger's equation at $Re = 6283$ and $c = 1$ with periodic boundary conditions using second-order finite differences and fourth-order compact differences.
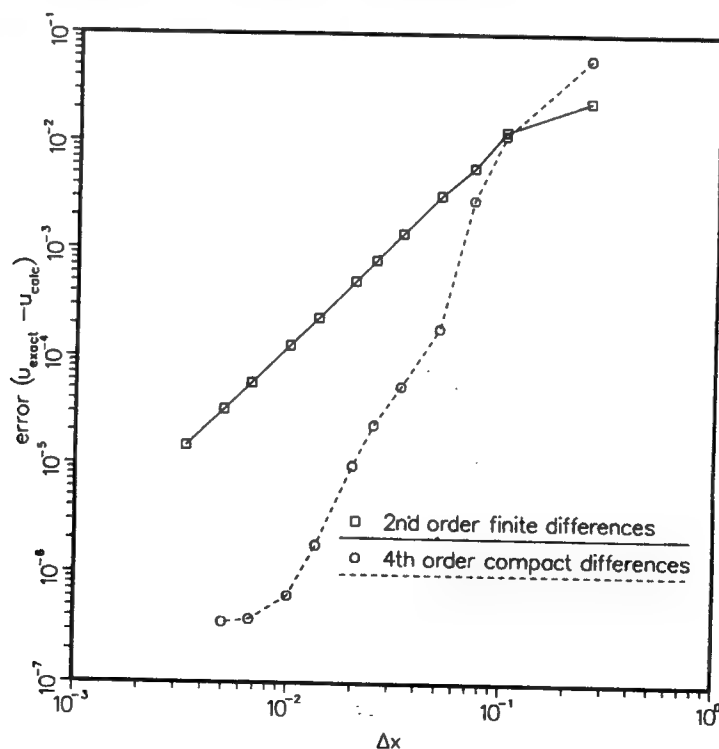
Figure 4: Error in computing the unsteady, nonlinear, viscous Burger's equation at $Re = 10$ and $u = c$ using second-order finite differences and fourth-order compact differences.
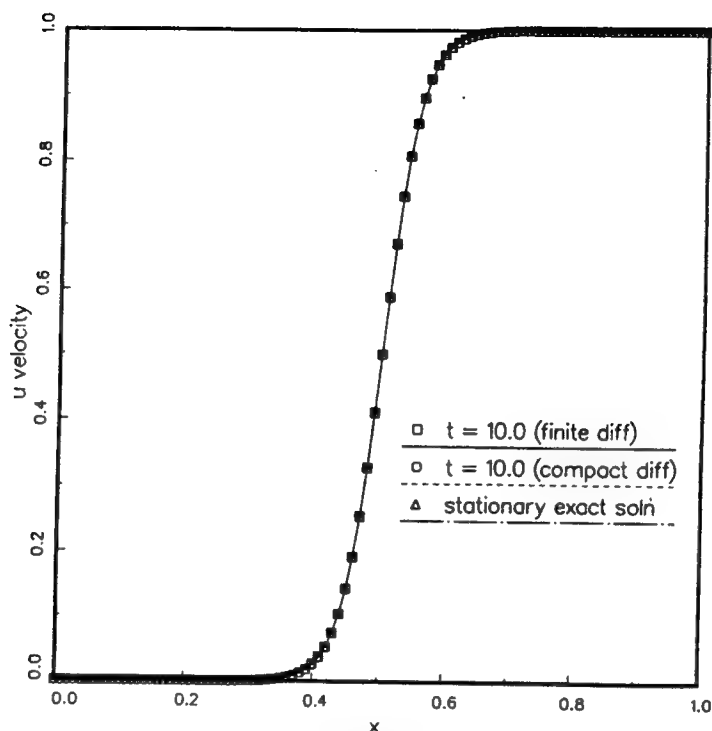
Figure 5: Comparison of exact solution with computed solution for the unsteady, nonlinear, viscous Burger's equation at $Re = 10$, $c = 0.5$, and $b = -1$ using second-order finite differences and fourth-order compact differences and $\Delta x = 0.01$.
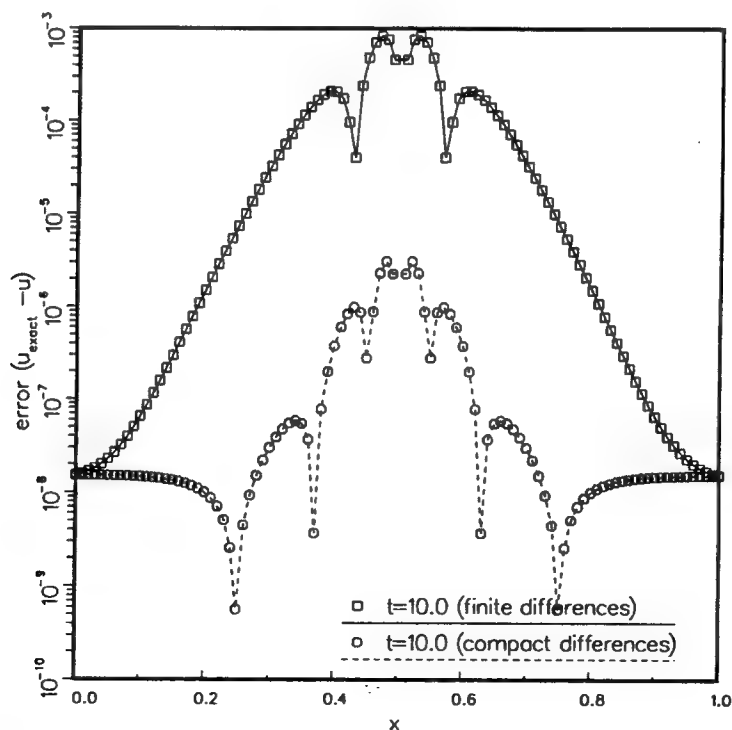
Figure 6: Spatial distribution of error for the unsteady, nonlinear, viscous Burger's equation at $Re = 10$, $c = 0.5$, and $b = -1$ using second-order finite differences and fourth-order compact differences and $\Delta x = 0.01$.
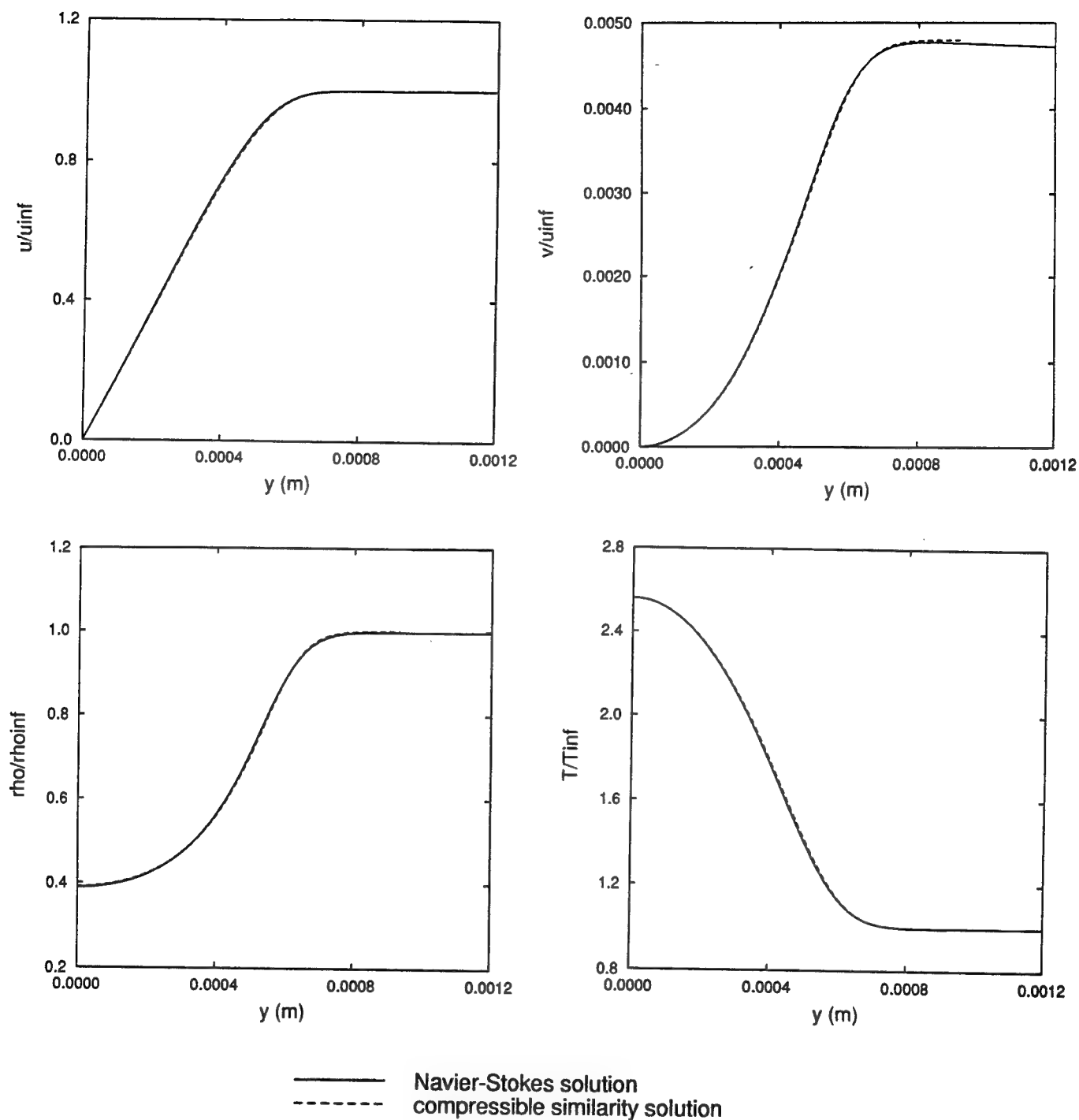
Figure 7: Comparison of laminar mean flow solution with the compressible similarity solution for a $M_\infty = 3$ flat plate boundary layer.
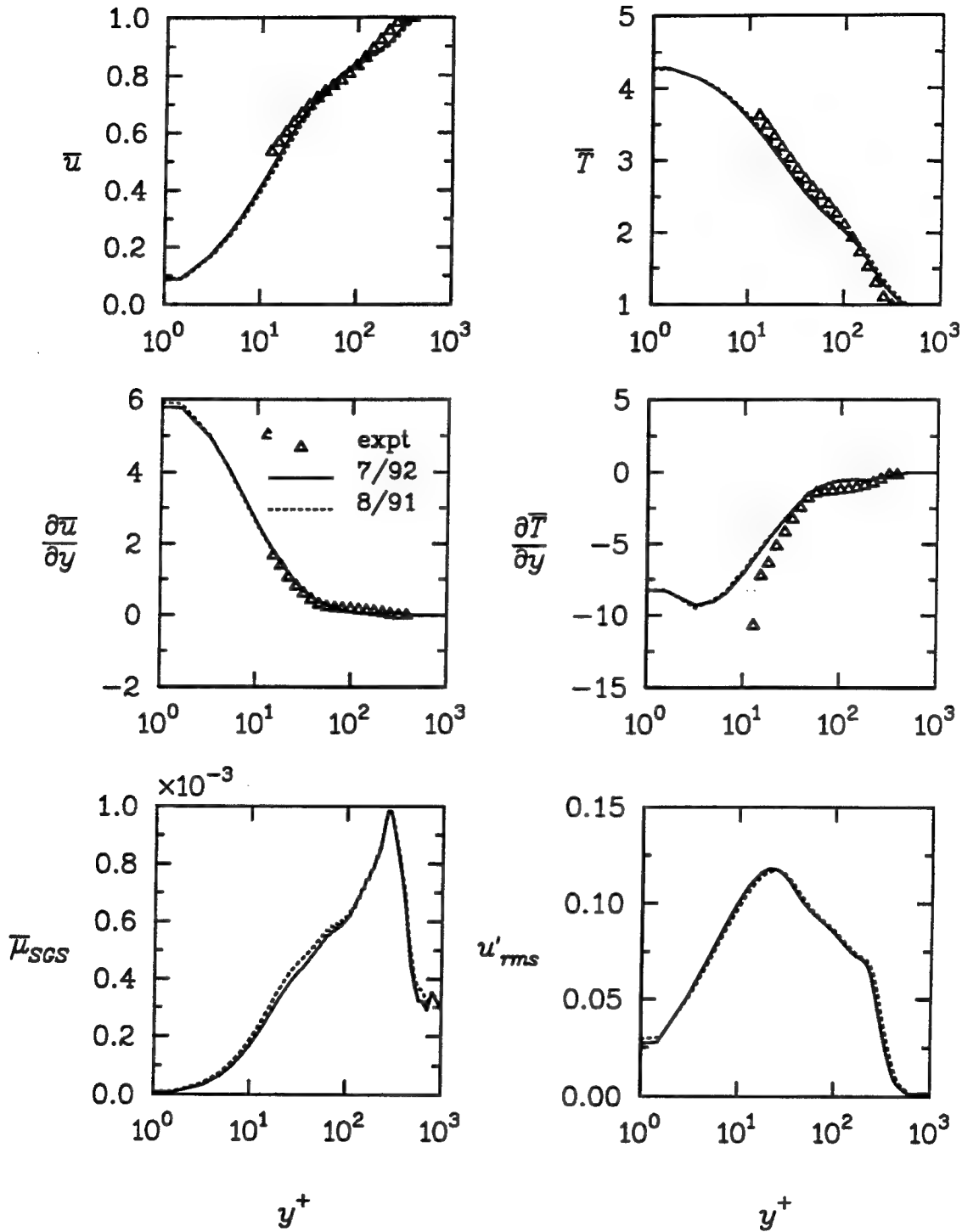
Figure 8: Influence of modifications in the high-order differencing scheme on the mean flow, the SGS viscosity, and the rms of the streamwise velocity using the compressible Smagorinsky SGS model ($c_r = 0.15$) for a temporal LES of a $M_\infty = 4.5$ turbulent boundary layer at $Re_\theta = 5400$. Comparison is shown with the experimental data of Coles (1953).
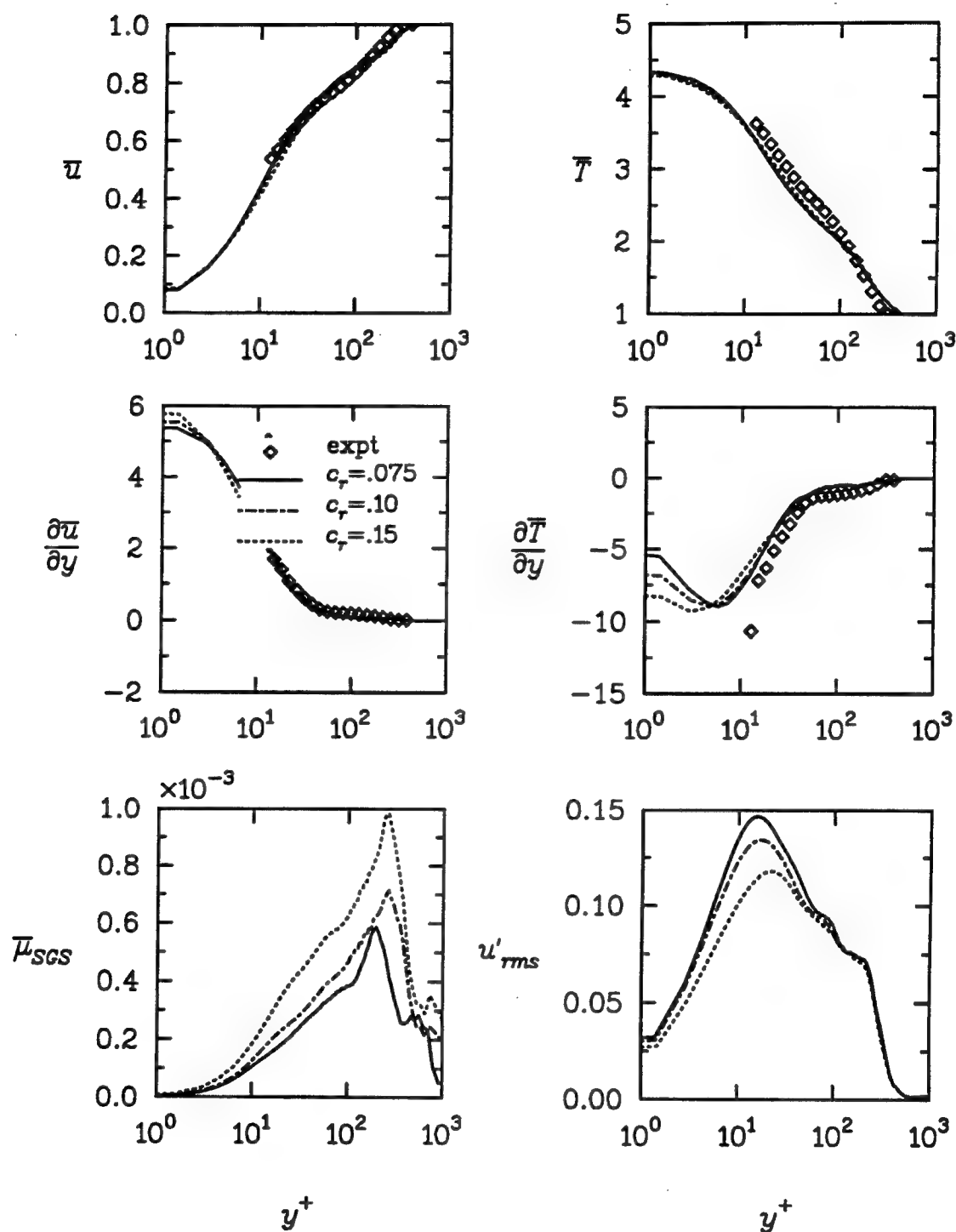
Figure 9: Influence of the compressible Smagorinsky constant on the mean and fluctuating flow of a supersonic turbulent boundary layer using the modified temporal LES code with the compressible Smagorinsky SGS model. Comparison is also shown with the experimental data of Coles (1953).
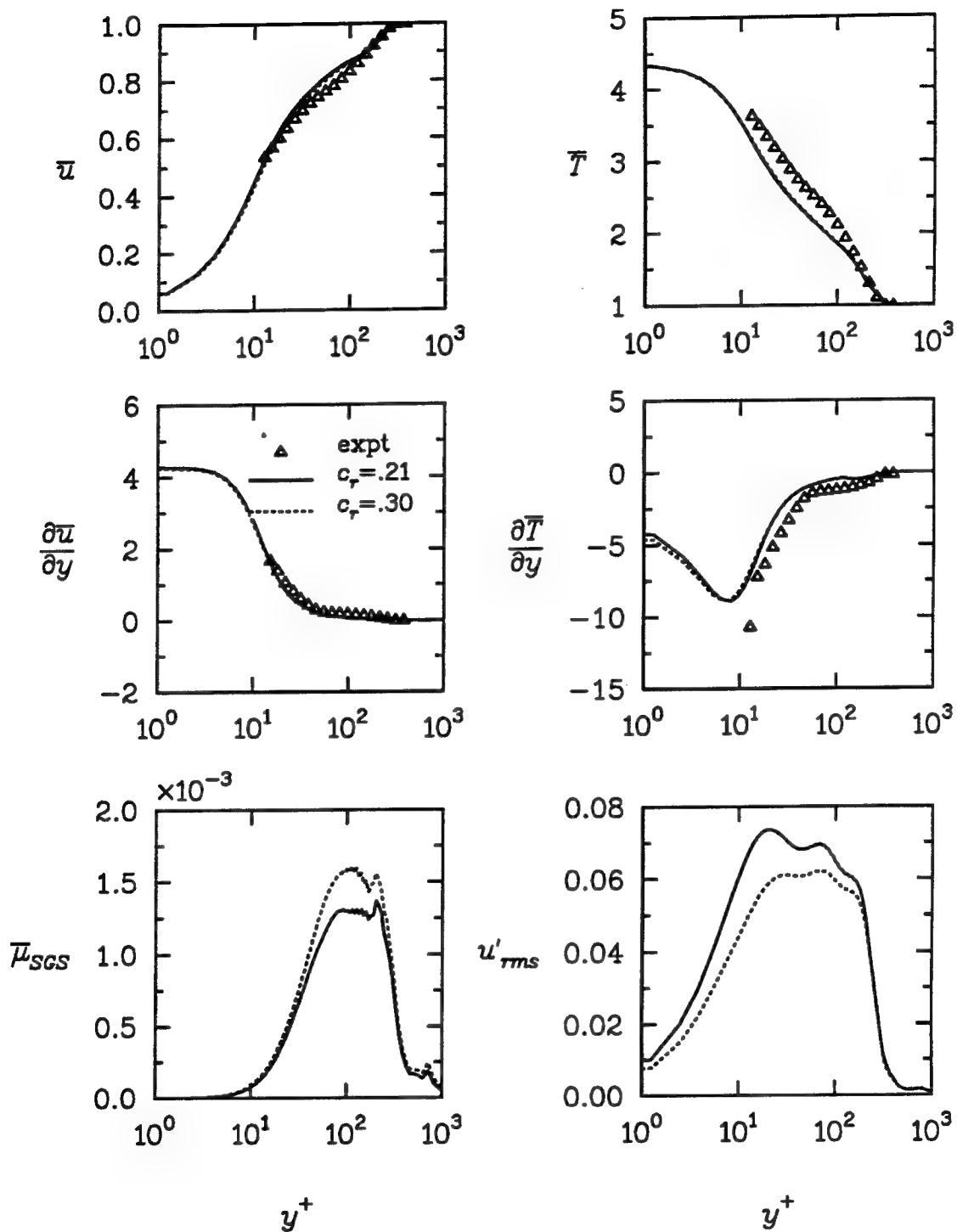
Figure 10: Influence of the compressible SGS constant on the mean and fluctuating flow of a supersonic turbulent boundary layer using the modified temporal LES code with the compressible structure function SGS model. Comparison is also shown with the experimental data of Coles (1953).
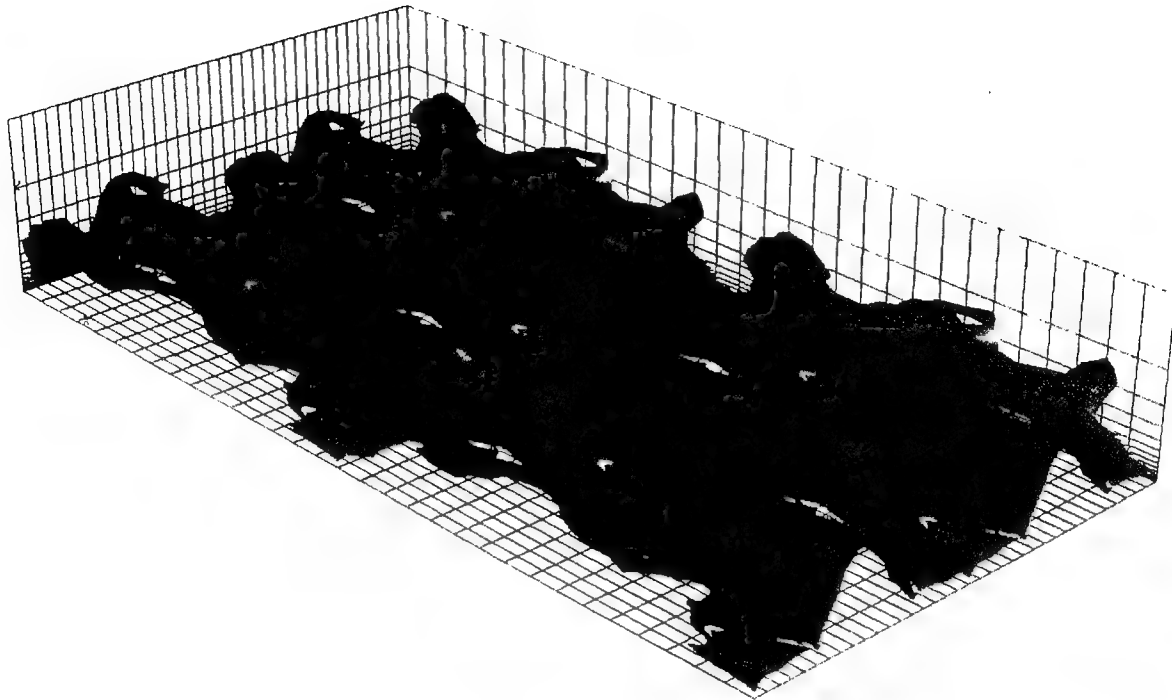
Figure 11: Constant density surface from a temporal LES of a supersonic turbulent boundary layer using the compressible Smagorinsky SGS model. Horseshoe-shaped structures are similar to those observed in experiments.
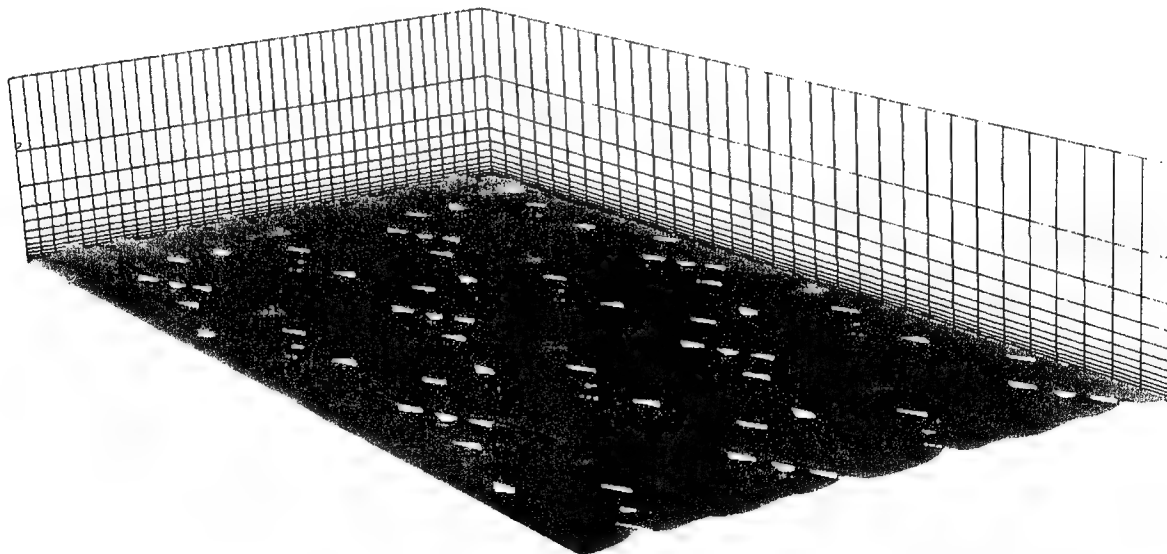
Figure 12: Low momentum (streamwise) fluid near the wall from a temporal LES of a supersonic turbulent boundary layer using the compressible Smagorinsky SGS model. Low-speed streaks are seen lifting away from the wall.

Density

0.00   0.50   1.00
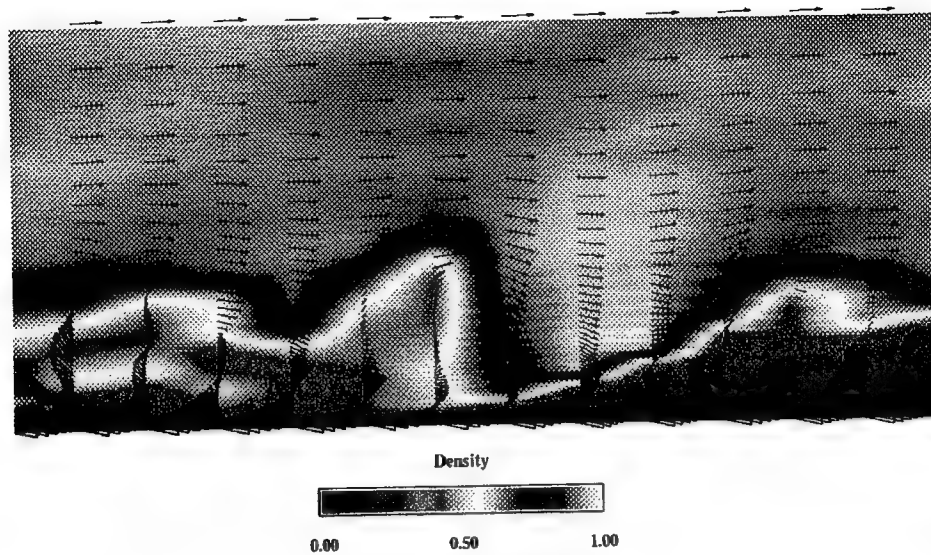
Figure 13: Velocity vectors and density contours identifying structural features in a Mach 4.5 turbulent boundary layer.
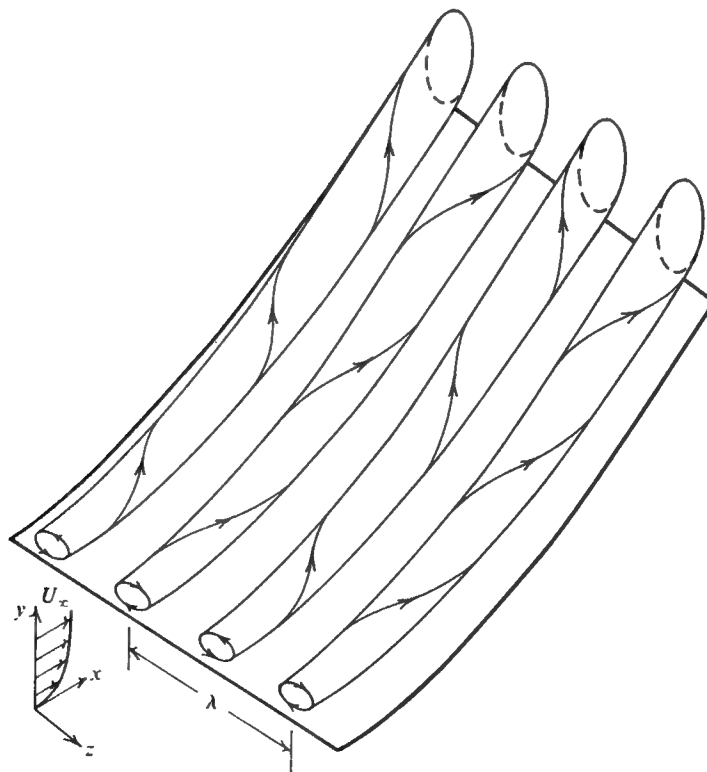
Figure 14: Sketch of the streamwise vortices developing on a concave wall due to the Görtler instability mechanism (from Swearingen and Blackwelder (1987)).
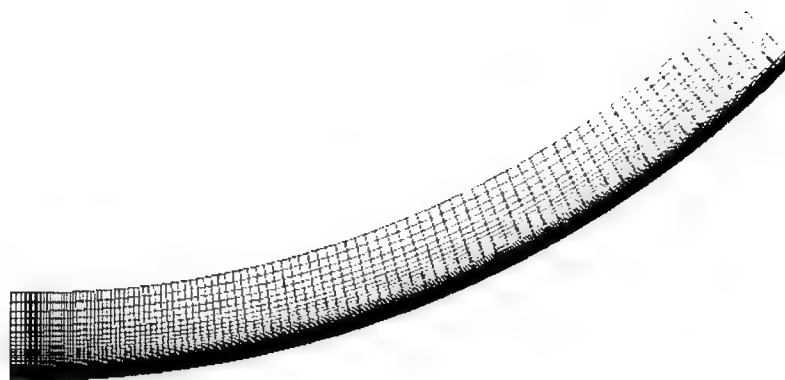
Figure 15: Computational grid for calculation of the Görtler instability.
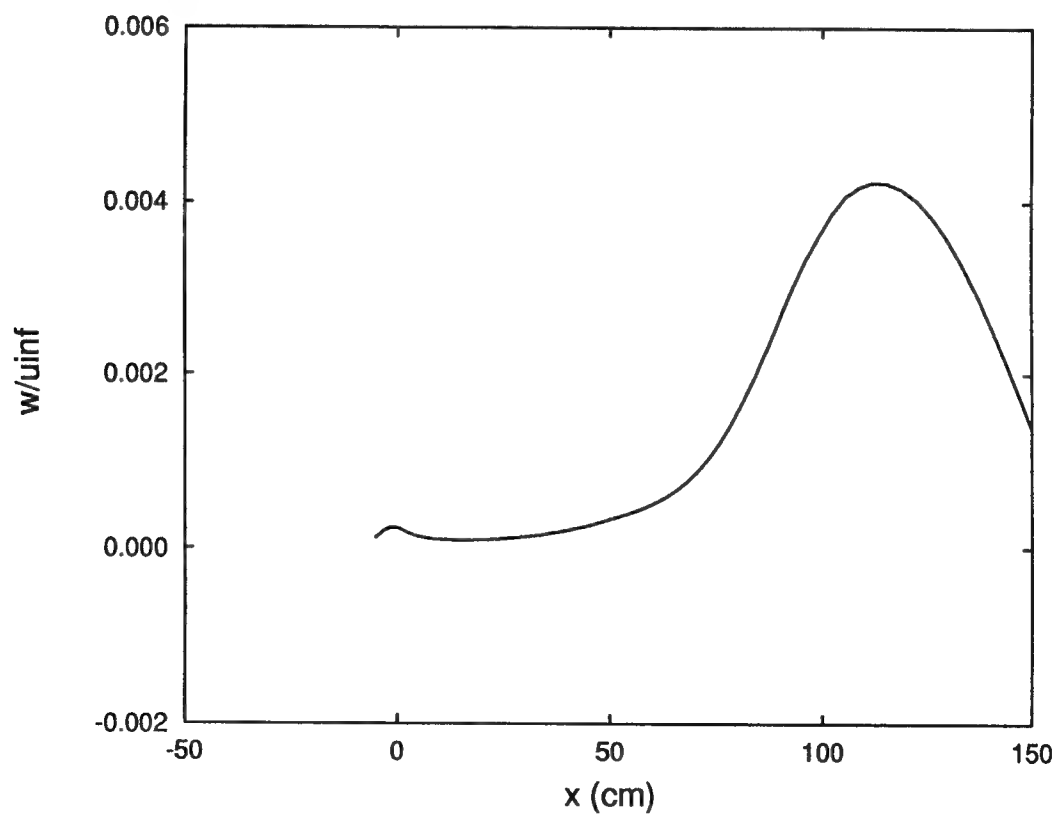
Figure 16: Downstream growth of the amplitude of the spanwise velocity near the wall at $y^+ \approx 10$.
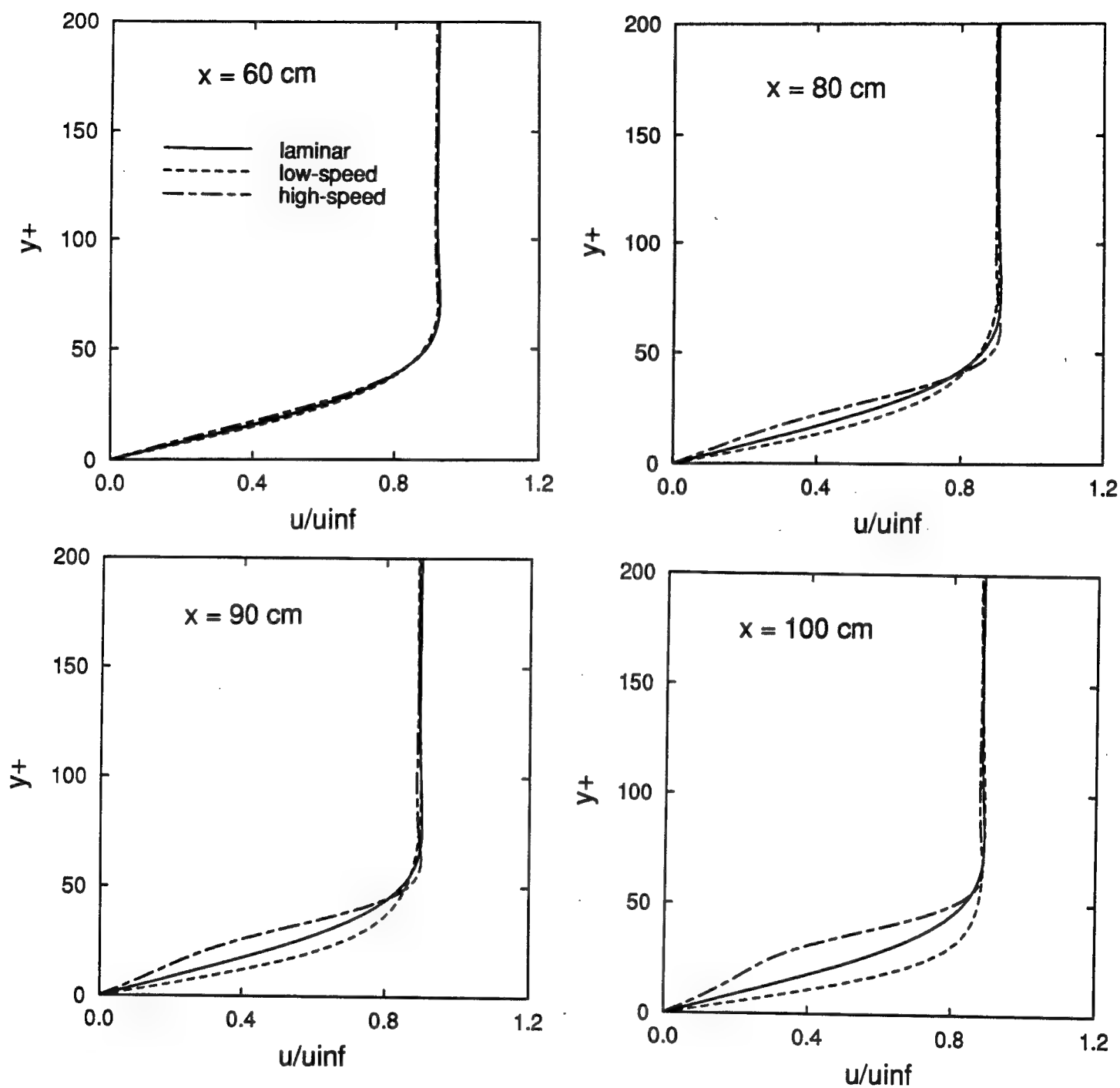
Figure 17: Normal profiles of the mean streamwise velocity with comparison to the laminar mean flow solution.
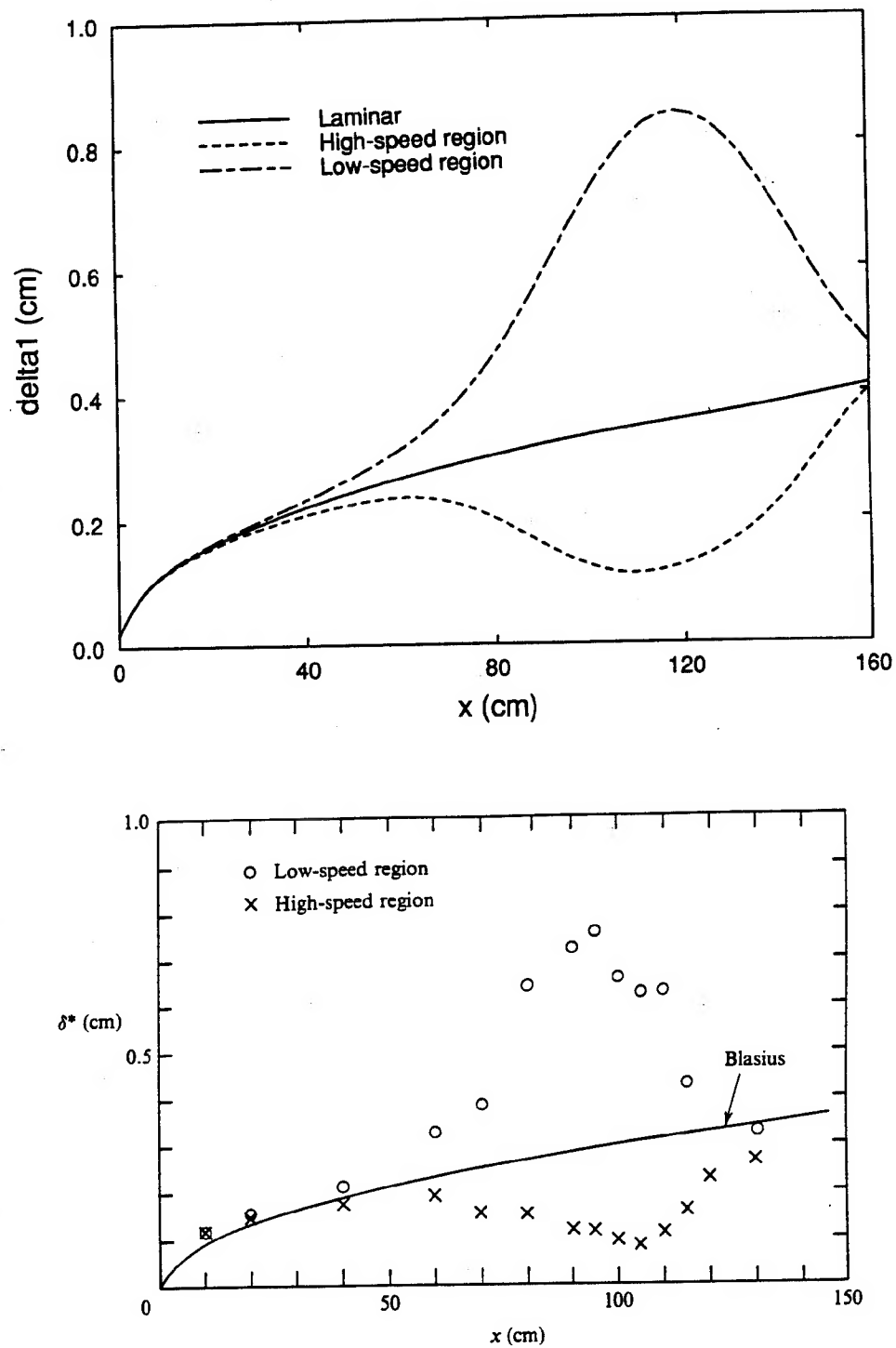
Figure 18: Downstream development of the displacement thickness in the low-speed and high-speed region. Also shown are the experimental measurements of Swearingen and Blackwelder (1987).
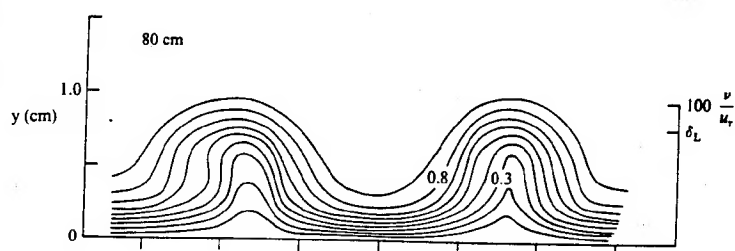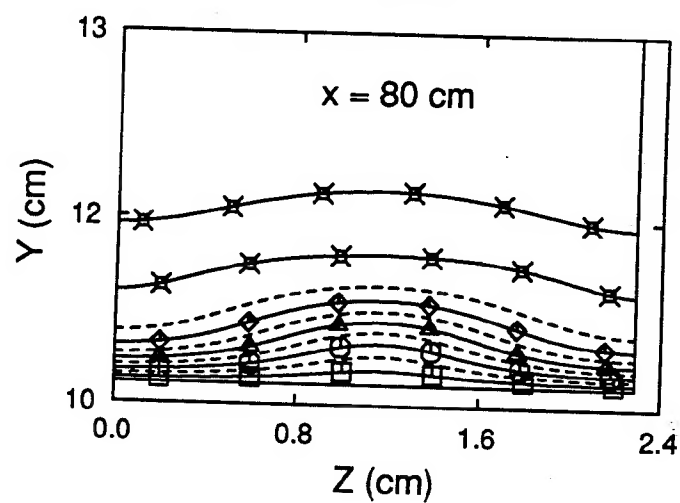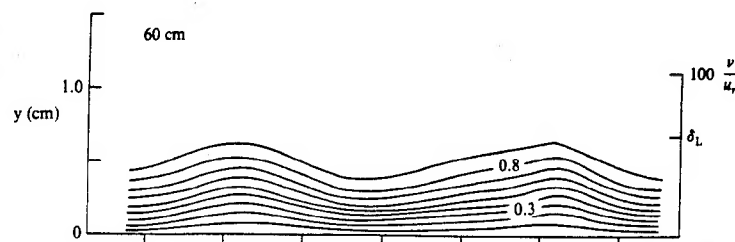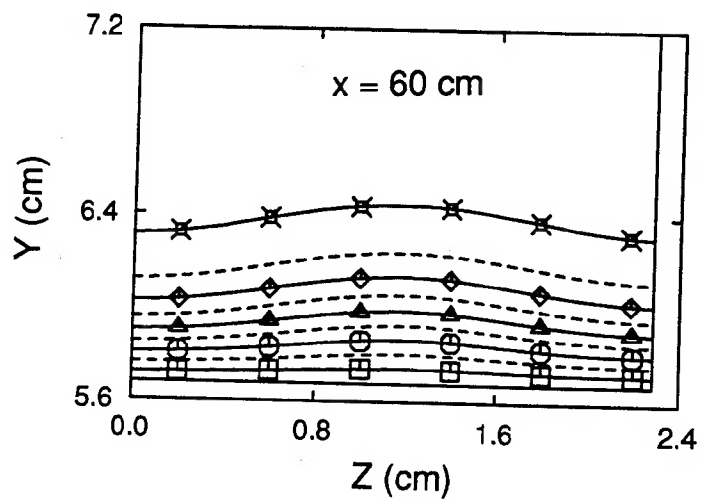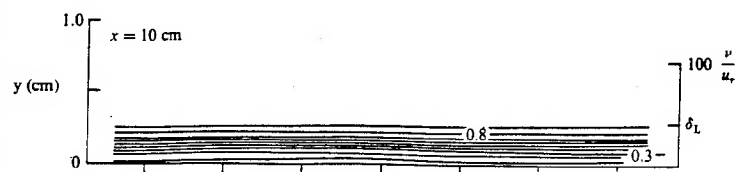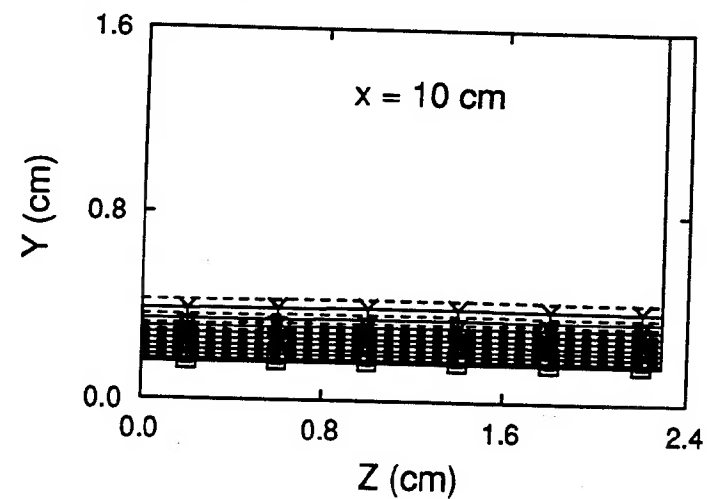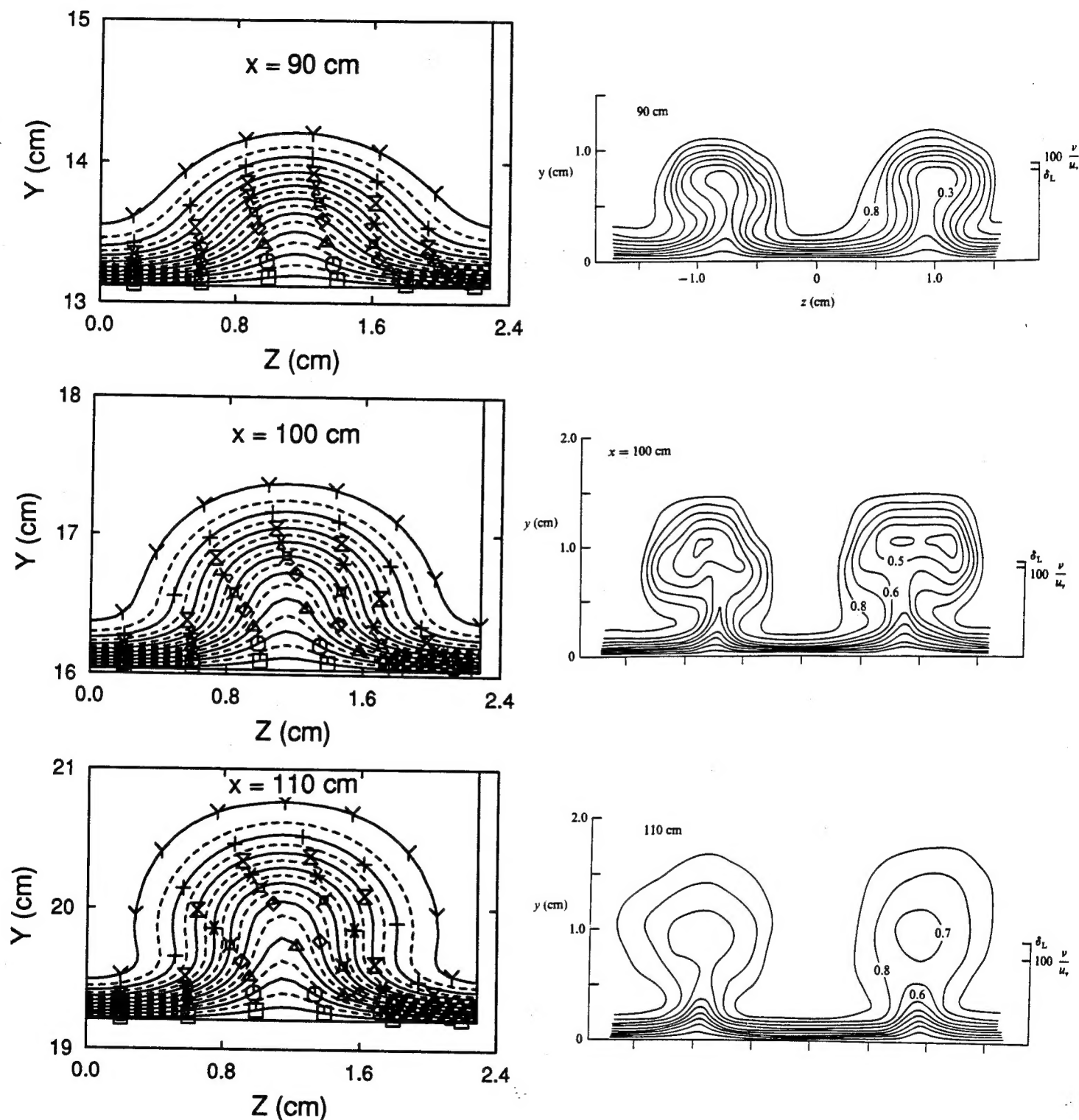
Figure 19: For caption, see following page.

Figure 19: Iso-contours of the mean streamwise velocity in the cross-stream (y, z)-plane for several streamwise x locations. Also shown on the right side are the experimentally determined contours of Swearingen and Blackwelder (1987).
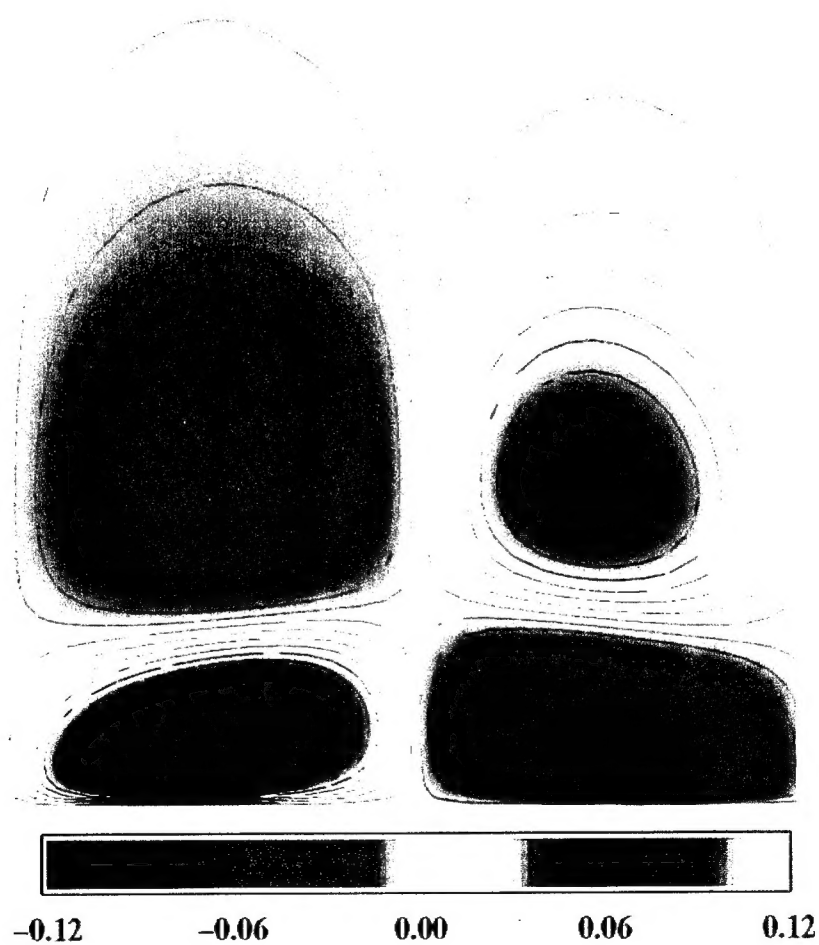
-0.12   -0.06   0.00   0.06   0.12

Figure 20: Iso-contours of the spanwise velocity at $x = 100$ cm showing the delelopment of counter-rotating vortices.